Online ISSN: 2981-0396 Print ISSN: 2981-0388

International Journal of Iron & Steel Society of Iran

Journal Homepage: https://journal.issiran.com/

Research Article

Induration Behavior of Iron Ore Pellets in A Pilot-Scale Packed Bed Furnace: A Computational Fluid Dynamics Approach

S. S. Razavi [1], E. Keshavarz Alamdari *[2]

Department of materials and Metallurgical Engineering, Amirkabir University of Technology, Tehran, Iran

ARTICLE INFO

Keywords:

Iron Ore Pelletization. Computational Fluid Dynamics (CFD), Radial Voidage Variation, Magnetite Oxidation, Wall Effect, Process Optimization.

Article history:

Received 02 March 2022
Received in revised form 22 September 2025
Accepted 06 May 2026

ABSTRACT

Iron ore pellets have emerged as the dominant burden material in modern ironmaking due to their uniform quality, superior mechanical strength, and enhanced transportability. The induration process, consisting of drying, preheating, firing, and cooling stages, is critical to achieving these desirable properties, with the firing stage being particularly important for pellet recrystallization and sintering. Among the key reactions, magnetite oxidation not only strengthens internal bonding by producing hematite but also contributes to the furnace's thermal balance. Ensuring complete conversion is essential to minimize residual FeO, which directly affects pellet reducibility and cold crushing strength (CCS). Pilot-scale packed-bed tests are commonly employed to simulate industrial firing conditions. However, these experiments can show high variability due to radial non-uniformity in voidage and gas flow. In the present study, experimental data revealed that, at corresponding heights, wall-adjacent pellets reached temperatures on average 60 °C higher than pellets in the center during the firing stage, with differences persisting for up to 23 minutes. This thermal disparity led to a higher conversion fraction near the walls by approximately 3–6 %, as determined by residual FeO measurements. Moreover, CCS tests on 35 carefully selected pellets indicated that lateral pellets exhibited strengths between 14 and 56 kg/pellet, higher than those of their central counterparts, depending on bed height. Such discrepancies are often overlooked in one-dimensional models, which assume uniform voidage and flow. In contrast, two-dimensional axisymmetric CFD modeling offers a more accurate representation by incorporating radial variations in voidage and accounting for magnetite oxidation reaction kinetics. In this study, the developed CFD model accurately reproduced the measured temperature profiles and conversion fractions, with a maximum deviation of less than 5 % from the pilot-scale experimental data. These findings underscore the importance of wall effects in small-to-medium induration setups, where the affected zone can account for a substantial portion of the bed volume. The distinct thermal histories of pellets in lateral versus central positions can mislead average property assessments if inappropriate sampling is employed. Therefore, integrating quantitative understanding of radial gradients into both modeling and operational practice is essential for accurate process optimization, scale-up, and quality control in iron ore pellet production.

** Corresponding Author*
Email: alamdari@aut.ac.ir
Address: Department of materials and Metallurgical Engineering, Amirkabir University of Technology, Tehran, Iran
1. Ph.D. Candidate, 2. Professor

DOI: http://10.22034/IJISSI.2026.549886.1221
Published by ISSI (Iron & Steel Society of Iran)

1. Introduction

Iron ore pellets have become the dominant feedstock in ironmaking due to their numerous advantages. These engineered marvels boast consistent properties, improved transportability, and superior mechanical strength, leading to increased production rates and efficiency [1]. Their creation involves a heat-hardening process known as induration, consisting of four key stages: drying, preheating, firing, and cooling. The firing stage plays a critical role, as it involves recrystallization and sintering that significantly enhance pellet strength.

A crucial reaction during induration is the oxidation of magnetite. This reaction not only contributes to the overall energy balance in the pelletizing plant but also leads to stronger bonding within the pellets, reducing dust generation during transport [2, 3]. Furthermore, ensuring complete conversion of magnetite to hematite is essential for proper firing and minimizing retained FeO. The final compressive strength and reducibility of the pellets are heavily influenced by the degree of magnetite oxidation [4].

Although pilot-scale packed-bed tests are widely used to predict industrial firing conditions, they often exhibit significant inconsistencies. The measured mechanochemical properties—particularly cold compressive strength and retained FeO—show large standard deviations at specific bed heights. This scattering is likely due to the non-uniform radial distribution of pellets within the pilot bed, leading to variations in their thermo-chemical history [5]. Simulating the evolution of pellet temperature and oxidation degree in both vertical and radial directions can offer valuable insights for addressing these inconsistencies.

Classic one-dimensional heterogeneous reactor models have been developed to simulate induration furnaces. However, these models are not accurate for packed beds due to the significant influence of wall effects [6, 7]. These effects lead to variations in bed voidage, which, in turn, influence critical parameters such as temperature and conversion fraction [6, 8, 9].

Researchers have explored incorporating radial velocity profiles into the models to address the limitations of 1D models [10, 11]. While this approach doesn't perfectly capture the actual velocity distribution, it leads to improved agreement with experimental results. CFD has been successfully applied to model heat transfer in packed beds involving phase-change materials and catalytic reactions [12, 13]. Notably, Nouri used a 2D model to compare temperature distributions in a blast furnace shaft under different burden modes [14]. At the same time, Pahlevaninezhad employed a 2D axisymmetric model to study the influence of operational parameters on the sintering process [15].

Understanding the underlying science behind iron ore pelletization is paramount in metallurgical engineering. The oxidation of magnetite concentrates, a critical stage during induration, significantly influences final pellet properties. The associated exothermic nature necessitates meticulous temperature control to prevent hematite dissociation, a detrimental reaction that weakens pellet integrity and disrupts reduction efficiency [16, 17, 18]. Kinetic studies employing advanced mathematical models play a crucial role in elucidating these reaction pathways and establishing optimal process parameters [19, 20, 21, 22, 23].

Process optimization in iron ore pelletization requires a delicate balance among multiple interacting parameters. The firing temperature, a critical factor governing pellet strength, must be precisely controlled to prevent excessive hematite dissociation and the associated deterioration of pellet integrity. Particle size distribution also plays a vital role, with an optimized range influencing packing density within the reduction reactor and subsequent gas flow characteristics [24, 25]. Computational tools such as CFD-DEM simulations provide valuable insights into these complex interactions, enabling metallurgists to optimize process parameters and enhance pellet quality and subsequent reduction efficiency [26, 27, 28, 29].

The industrial landscape of iron ore pelletization underscores the critical role of pellet production in modern ironmaking. Mathematical models can be harnessed to optimize the operation of pellet induration furnaces, ensuring consistent production of high-quality pellets with optimal reducibility characteristics [30]. Preheating processes can further enhance reduction efficiency by removing moisture and preheating the pellets before entering the reduction [31].

The future of iron ore pelletization is brimming with exciting possibilities. High-temperature reduction processes offer a glimpse of a more sustainable future, potentially enabling the production of high-quality iron feedstock with a minimal environmental footprint [19]. Additionally, advancements in particle size distribution optimization can unlock the full potential of various iron ore concentrates, thereby promoting resource utilization efficiency [25].

While simulations of the pellet induration process in pilot-scale plants have shown considerable promise [32], continued research is required to achieve comprehensive process optimization. This research proposes a novel approach for evaluating iron ore pellet induration in a pilot-scale furnace equipped with Outotec induration technology at Golgohar Mining & Industrial Co. The core innovation is the use of Computational Fluid Dynamics (CFD) modeling, which overcomes the inherent limitations of conventional one-dimensional models. This CFD model incorporates two critical aspects often neglected in prior studies: voidage variation and reaction kinetics. The voidage variation equation captures the non-uniform packing density of pellets within the furnace, a phenomenon that significantly influences heat

transfer and reaction kinetics [6, 7, 8, 9]. Traditional models assume uniform voidage, leading to inaccuracies. The model also incorporates the kinetics of magnetite oxidation reaction, a fundamental step in induration that governs the final pellet properties [2, 3, 4]. This inclusion enables the prediction of temperature profiles and the degree of magnetite conversion within the pellets. The CFD model's capability to resolve three-dimensional flow fields within the furnace geometry yields a more accurate representation of gas flow patterns than conventional one-dimensional models [6, 8, 9]. A precise understanding of the flow field is essential for predicting how heat transfer and chemical reactions interact within the packed bed of pellets. The predicted temperature profiles and final conversion fractions from the CFD model will be validated against actual data from the Outotec induration furnace. This validation ensures the model's accuracy and ability to represent the complex interplay of heat transfer, chemical reactions, and gas flow within the furnace.

This innovative CFD approach offers significant advantages for the field of iron ore pelletization. By incorporating voidage variations, reaction kinetics, and 3D flow fields, the model provides a more holistic picture of the induration process. This comprehensive understanding can be harnessed for various metallurgical engineering applications, including process optimization, scale-up considerations for industrial furnaces, and potentially reduced pilot testing requirements. This research signifies a significant advancement in iron ore pelletization modeling and paves the way for more efficient, optimized, and sustainable pellet production.

2. Governing Equations and Numerical Procedure

2.1. Conservation Equations

The governing equations for the gas phase are based on mass and momentum balances, including the effect of local voidage ($\varepsilon_{(r)}$). These equations are expressed as follows:

Eq.(1)

$$\frac{\partial \varepsilon_{(r)}\rho_g}{\partial t} + \nabla \cdot (\rho_g \mathbf{u}) = \dot{R}_i \;\&\; i = O_2, CO_2$$

Eq.(2)

$$\frac{\partial \rho_g \mathbf{u}}{\partial t} + \nabla \cdot (\rho_g \mathbf{u}\mathbf{u}) + \nabla P - \nabla \cdot (\mu \nabla \mathbf{u}) = S_m$$

Where $\varepsilon_{(r)}$ is the local bed voidage (–), ρ_g is the gas density (kg·m^{-3}), **u** is the superficial gas velocity vector (m·s^{-1}), Ṙ is the source/sink term for species i (kg·m^{-3}·s^{-1}), P is the gas pressure (Pa), μ is the gas viscosity (Pa·s), and S_m is the mass source term due to chemical reactions (kg·m^{-3}·s^{-1}). The source term on the right-hand side of Eq.(1) is related to the gaseous phase production or consumption during the magnetite oxidation/decomposition reactions.

In Eq.(2), S_m can be modeled by the Ergun equation:

Eq.(3)

$$S_m = \frac{150\mu(1-\varepsilon_{(r)})^2 \mathbf{u}}{d_p^2 \varepsilon_{(r)}^3} + \frac{1.75\rho_g(1-\varepsilon_{(r)})|\mathbf{u}|\mathbf{u}}{d_p \varepsilon_{(r)}^3}$$

Where d_p is the pellet diameter (m). The realizable k-ε model was used to account for turbulence, as it has been successfully validated in similar reactors [33]. Since the thermal condition is non-equilibrium, two energy equations are considered for the solid and gas phases:

Eq.(4)

$$\left(1-\varepsilon_{(r)}\right)\left(\rho_P c_{P,P}\right)\frac{\partial T_P}{\partial t} = \left(1-\varepsilon_{(r)}\right)\nabla.\left(\lambda_{b,eff}\nabla T_P\right) + \left(1-\varepsilon_{(r)}\right)\sum R_i \& H_i + Ah^*(T_g - T_p)$$

Eq.(5)

$$\varepsilon_{(r)}(\rho_g c_{P,g})\frac{\partial T_g}{\partial t} + (\rho_g c_{Pg})\mathbf{u}\cdot\nabla T_g = \varepsilon_{(r)}\nabla(\lambda_{g,eff}\nabla T_g) + Ah_c(T_p - T_g)$$

Where ρ_p is the pellet density (kg·m^{-3}), c_p is the pellet heat capacity (J·kg^{-1}·K^{-1}), T_P is the pellet temperature (K), H_i is the heat of reaction (J·mol^{-1}), h* includes both convective and radiative heat transfer coefficients (W·m^{-2}·K^{-1}), T_g is the gas temperature (K), ρ_g is the gas density (kg·m^{-3}), $c_{p,g}$ is the gas specific heat capacity (J·kg^{-1}·K^{-1}), and h_c is the overall heat transfer coefficient (W·m^{-2}·K^{-1}). The following expression gives the specific surface area:

$$A = \frac{6(1-\varepsilon_{(r)})}{d_P} \quad \text{Eq.(6)}$$

A widely adopted approach for treating radiant heat transfer is to account for it in the convective heat transfer formulation [34]. Accordingly, the following empirical relation is used to determine the convective heat transfer coefficient, h_c:

$$Nu = 2.0 + 0.39 Re_p^{1/2} Pr^{1/3} \quad \text{Eq.(7)}$$

Additionally, the correlation proposed by Schotte [35] is used to determine the radiative heat transfer coefficient, h_{rad}:

$$h_{rad} = 0.692\, exp\left(\frac{T^3}{10^8}\right) \quad \text{Eq.(8)}$$

The conservation equation for the gaseous species in the bed is expressed as:

Eq.(9)

$$\frac{\partial \varepsilon_{(r)} \rho_g Y_i}{\partial t} + \mathbf{u} \cdot \nabla(\rho_g Y_i) - \nabla \cdot (\varepsilon_{(r)} \rho_g D_i \nabla Y_i) = \dot{R}_i \;\&\; i = O_2, CO_2$$

Where Y_i is the mass fraction of species i(–), D_i is the Diffusion coefficient of species i ($m^2 \cdot s^{-1}$).

2.2. Kinetic and Thermodynamic Model

The Unreacted Shrinking Core Model (USCM) is applied to express the reaction rate based on a mixed control mechanism in the following form [36]:

Eq.(10)

$$\frac{dr_{mag}}{dt} = \frac{-(C_{O_2} - C^e_{O_2})}{\frac{\rho_{mag}}{4}\left[\frac{r_p^2}{r_{mag}^2 k_{O_2}} + \frac{r_{mag}^2}{D_{O_2,eff}}\left(\frac{1}{r_{mag}} - \frac{1}{r_p}\right) + \frac{1}{k'_{mag}}\right]}$$

Where r_{mag} is the radius of the magnetite pellet (m), C_{O_2} is the oxygen concentration in the gas ($kg \cdot m^{-3}$), $C^{eq}_{O_2}$ is the equilibrium oxygen concentration in the gas ($kg \cdot m^{-3}$), ρ_{mag} is the magnetite density ($kg \cdot m^{-3}$), k_{1st} is the first-order rate constant for magnetite oxidation (s^{-1}) (obtained from Thurlby[37]), and D_{O_2} is the oxygen Diffusion coefficient, which can be obtained by analogy with heat transfer:

$$Sh = 2.0 + 0.39 Re_p^{1/2} Sc^{1/3} \qquad \text{Eq.(11)}$$

In Eq.(10), $D_{O_2,eff}$ is the oxygen effective diffusivity in the pellet, which consists of two terms:

$$\frac{1}{D_{O_2,eff}} = \frac{1}{\varepsilon_p^2}\left(\frac{1}{D_{O_2}} + \frac{1}{D_K}\right) \qquad \text{Eq.(12)}$$

Where D_{O_2} is the molecular diffusivity of oxygen, as stated by the Chapman-Enskog relation [38], and D_{Kn} is is the Knudsen diffusivity, which is dominant in the micropores and can be estimated as follows [14]:

$$D_K = \frac{4}{3}\left(\frac{8RT}{\pi M_{O_2}}\right)^{1/2} \cdot \frac{3\pi r_g}{4(\pi+8)(1-\varepsilon_p)} \qquad \text{Eq.(13)}$$

Where r_g is the pore radius (m), R is the universal gas constant ($J \cdot mol^{-1} \cdot K^{-1}$), and M is the molar mass ($kg \cdot mol^{-1}$).

2.3. Voidage Variation

The radial voidage variation in the bed is modeled with the empirical Equation by de Klerk [39]. De Klerk derived an equation for voidage variation by mono-sized spheres. The Equation gives the radial voidage for different packing ratios (d_b/d_p) as a function of the normalized wall distance:

Eq.(14)

$$\varepsilon_{(r)} = \begin{cases} 2.14z^2 - 2.53z + 1, & z \le 0.637 \\ \varepsilon_0 + 0.29\, exp(-0.6z) \cdot [cos(2.3\pi (z - 10.16))] + 0.15\, exp(-0.9\, z), & z > 0.637 \end{cases}$$

$$\varepsilon_0 = 0.379 + \frac{0.078}{(\frac{d_b}{d_p} - 1.8)} \qquad \text{Eq.(15)}$$

where $z = (r_b - r)/d_p$ and ε_0 are respectively the normalized distance from the wall and the bed voidage far away from the wall.

2.4. Numerical Procedure

The solution process employed the finite-volume method in the OpenFOAM code. A two-dimensional axisymmetric mesh was used. The discretized equations were solved using the geometric algebraic multigrid (GAMG) method with a Gauss-Seidel smoother. The pressure-velocity coupling was achieved with the pressure implicit split operator (PISO). Amani et al. [23, 28, 29] addressed the details of the numerical procedure, initial and boundary conditions, assumptions, mesh dependency, and other relevant considerations. The kinetic models were described in previous works [18, 24]. Amani et al. [23, 28, 29] presented a merged model incorporating elements from these and other sources. Simulations were performed using OpenFOAM v8 on Ubuntu 20.04, CPU: Intel Xeon E5-2650 v4 @ 2.20 GHz, RAM: 64 GB. The average simulation time for each run was approximately 7 hours.

2.5. Experimental Method

Fig. 1. illustrates the reactor design and boundary conditions employed in the model. The reactor is a packed-bed cylindrical geometry measuring 26.5 cm in diameter and 80 cm in height. It's divided into four distinct sections:

Upper Hood (10 cm): This section facilitates controlled entry and exit of gases during the reaction.

Reaction Zone (35 cm): This is the heart of the reactor, where the primary chemical transformation of the iron ore pellets occurs.

Hearth Layer (10 cm): This layer, composed of inert material, serves a critical purpose – it protects the grate bars at the bottom of the reactor from the high temperatures generated during the reaction.

Wind Box (15 cm): Similar to the upper hood, this section provides another designated area for gas inflow and outflow.

The reactor is filled with pre-dried iron ore pellets, boasting an average porosity of 31%. These pellets were meticulously screened to achieve a uniform size

of approximately 1.2 cm. The composition of the pellets involves a blend of 80 wt.% high magnetite concentrate and 20 wt.% low magnetite concentrate. This translates to an FeO content of 24.67 wt.% for the high concentrate, 6.97 wt.% for the low concentrate, and a resulting blend composition of 21.13 wt.%.

For temperature monitoring, three thermocouples were strategically positioned along the vessel's central axis: P_1, P_2, and P_3. P_1 is located at the highest point, 42 cm from the bottom of the hearth layer. P_2 follows at a mid-point position, 27.5 cm from the hearth bottom. Finally, P_3 is the lowest, at a distance of 11 cm from the hearth layer. The temperatures recorded at these points are denoted T_1, T_2, and T_3, respectively, and were measured at predetermined intervals throughout the experiment, encompassing the preheating, firing, after-firing, and cooling phases.

3. Results and Discussion

3.1. Model Validation

Fig. 2(a). details the thermal cycle employed during the iron ore pellet firing process. The initial preheating Stage introduces hot air (973 K) for 2 minutes, followed by a rapid temperature increase (3 seconds) to the firing temperature of 1473 K. This high temperature is maintained for 8 minutes to achieve the desired thermal treatment within the pellets. Subsequently, the after-firing Stage lowers the temperature to 1273 K for 2 minutes, providing a controlled cooling step. Finally, the cooling Stage actively removes heat by introducing cooler air, reducing the temperature to 298 K over 5 minutes and then maintaining that temperature for an additional 5 minutes.

Fig. 2(b). compares the simulated and experimentally measured temperature profiles at points P_1 (top), P_2 (middle), and P_3 (bottom) within the reactor bed. The results demonstrate good overall agreement, validating the model's ability to predict temperature variations during the firing process. However, minor discrepancies are observed, particularly during the preheating and cooling stages. These deviations can be attributed to factors such as the inherent complexities of real-world heat transfer and slight variations in the actual properties of the iron ore pellets relative to the model's assumptions. The mean relative error (MRE) between the predicted and measured temperatures was also calculated for the three thermocouple positions (T_1, T_2, and T_3). The values ranged from 2.8% to 4.6%, confirming the model's good predictive accuracy. Analyzing the temperature profiles across the different stages offers valuable insights into the heat transfer dynamics within the reactor:

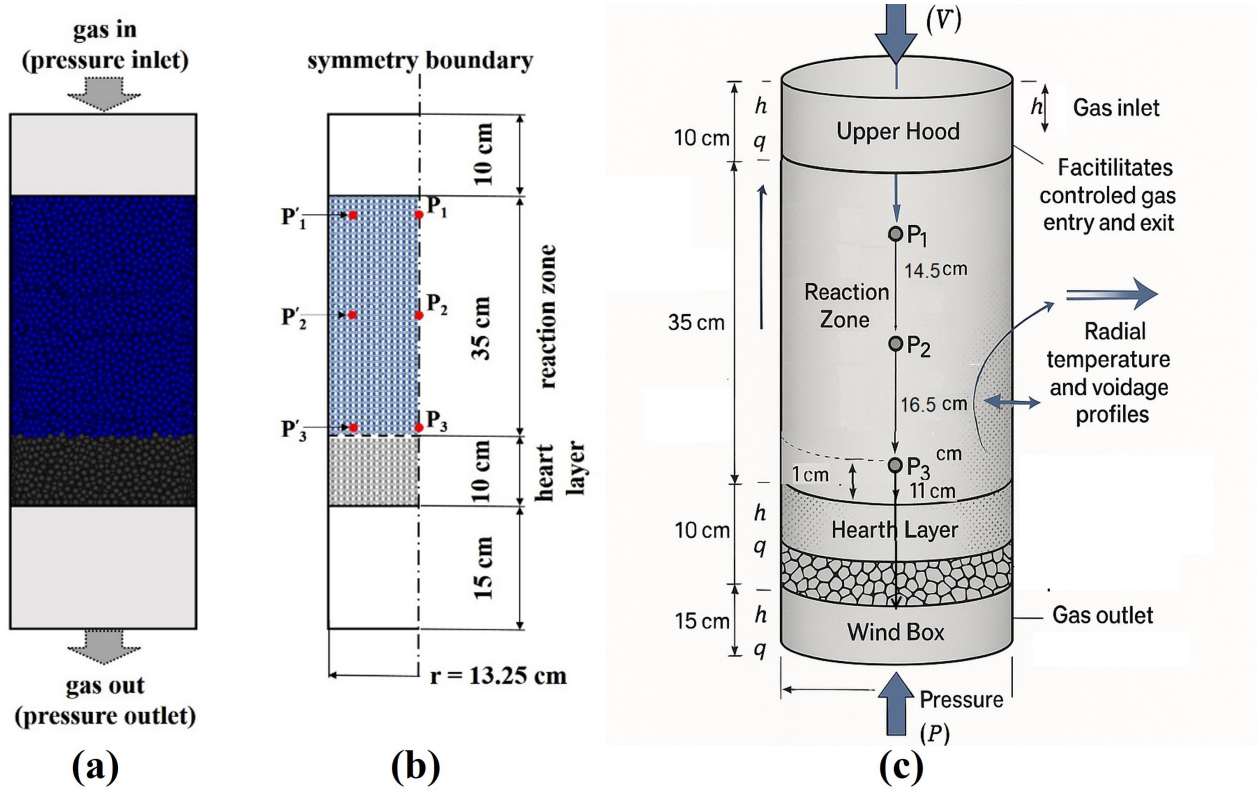

Fig. 1. (a) Schematic of the packed bed reactor, (b) Boundary conditions, (c) Computational Domain. The near wall points (P'_i) are the points with a distance of 1/4 bed radius from the wall at the same height as the corresponding axial points (P_i).

Preheating: During this initial Stage, the temperature gradually increases from the top (P_1) downwards (P_2, P_3) as the hot gas progressively heats the pellet layers sequentially. Optimizing the preheating duration enables control over the initial temperature profile in the bed.

Firing: Introducing high-temperature gas (1473 K) leads to a rapid rise in temperature at P_1 towards a steady state. However, the lower layers (P_2, P_3) experience a delay in reaching their peak temperatures due to the gradual heat transfer through the packed bed. Optimizing the firing duration is crucial for achieving the desired level of heat penetration throughout the pellet bed.

After Firing: The introduction of cooler air during the after-firing Stage initiates a controlled cooling process. P_1 cools first, releasing heat that transiently warms the lower sections (P_2, P_3). The duration of this Stage can be adjusted to control the cooling rate in the upper layers.

Cooling: Reversing the airflow direction with a positive pressure difference promotes forced cooling in the final Stage. As long as the air temperature remains lower than the pellets, P_2 and P_3 cool steadily. However, if the air temperature exceeds the pellet temperature, it can lead to a temporary rise in P_1's temperature, as observed in the simulation results. The cooling duration and air temperature are critical factors influencing the final temperature distribution within the pellet bed.

These observations on heat transfer dynamics provide valuable pointers for optimizing reactor performance. By carefully controlling factors such as gas temperature, flow rate, and the duration of each process stage (preheating, firing, after-firing, and cooling), we can achieve the desired temperature profiles within the reactor bed for efficient processing of iron ore pellets. Further discussion on the implications of these findings for process optimization will be presented in a subsequent section.

A key strength of this simulation is its ability to model the kinetic behavior of magnetite oxidation. This exothermic reaction significantly affects the reactor's thermal balance. However, directly measuring and analyzing the remaining FeO (unconverted magnetite) during the process is impractical. Only the final amount of FeO can be determined. Therefore, comparing the simulated and experimentally measured FeO content at the end of the process provides a valuable validation of the simulation's accuracy.

Fig. 3. presents the simulation results alongside the experimental data for the conversion fraction of magnetite (remaining FeO) at the end of the process, measured at points P_1 (top), P_2 (mid), and P_3 (bottom) within the reactor bed. As shown in the figure, the simulation results

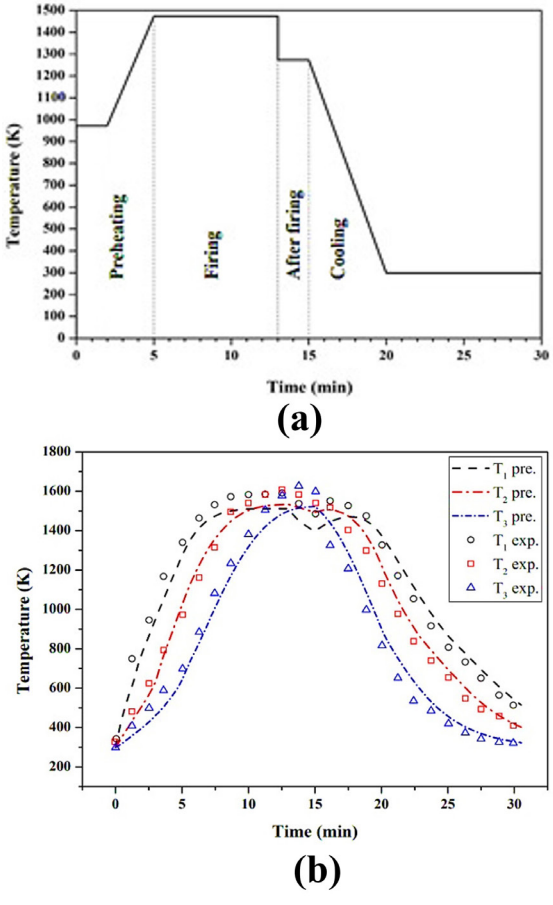

Fig. 2. (a) Inlet gas temperature profile for the validation test; (b) Comparison between measured and predicted temperature profiles in a pilot induration test.

and experimental data agree well within the limits of experimental error. This close correlation suggests that the simulation accurately predicts the magnetite conversion fraction. Furthermore, the simulation provides a valuable in-situ view of reaction progress at different locations within the reactor bed throughout the process, offering insights beyond what can be obtained from final-stage measurements alone.

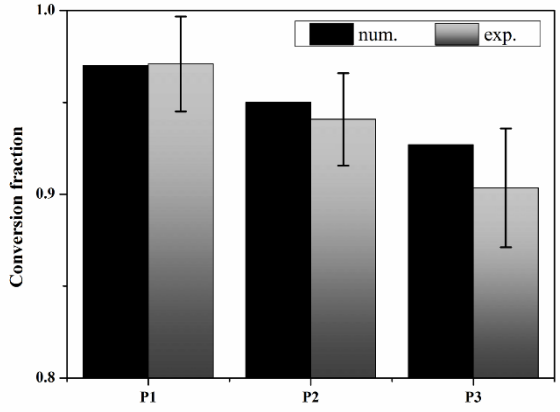

Fig. 3. Comparison of numerical and experimental values of conversion fraction at the end of induration.

Fig. 4. provides valuable insights into the spatial and temporal variations in magnetite conversion within the reactor bed, as observed in the simulation results. The conversion fraction of magnetite (remaining FeO) is plotted against time for points P_1 (top), P_2 (mid), and P_3 (bottom).

The initiation of magnetite oxidation exhibits a distinct spatial dependence. Oxidation commences at P_1 (top) after one minute, followed by P_2 (mid) at two minutes. Notably, P_3 (bottom) shows no signs of oxidation until the firing stage begins. This staggered reaction initiation can be attributed to the preheating Stage's temperature profile. The hotter top layers (P_1 and P_2) reach the activation temperature for magnetite oxidation earlier compared to the cooler bottom layer (P_3).

During the preheating Stage, P_1 and P_2 experience significant magnetite conversion (approximately 0.65 and 0.45, respectively). This early conversion highlights the impact of the preheating profile on reaction progress.

The firing stage shows continued oxidation in P_1 and P_2, while P_3 finally initiates its conversion. By the end of firing, most of the magnetite has been converted to hematite across all layers. The after-firing and cooling stages exhibit minimal changes in the conversion fraction, indicating minimal further reaction at this point.

These observations emphasize the importance of accounting for both spatial and temporal variations in temperature for a comprehensive understanding of reaction kinetics in packed-bed reactors. By carefully designing the thermal profile throughout the reactor bed and across different stages, we can optimize the conversion efficiency of magnetite to hematite during iron ore pellet processing.

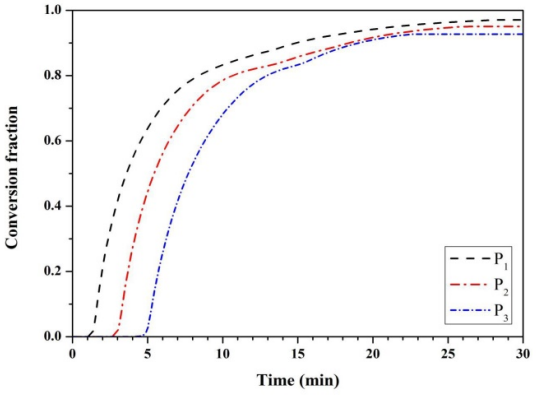

Fig. 4. Predicted magnetite oxidation fraction over time.

3.2. Effect of Radial Voidage Variation

Drawing upon the findings of De Klerk (1938) [39], Fig. 5. illustrates the radial voidage variation within the reactor bed for homogenous pellet particles of different diameters. As shown in the figure, the voidage (space) near the reactor wall exhibits significant fluctuations extending inward by up to 5 cm, corresponding to roughly 5 pellet diameters. This phenomenon, known as the "wall effect," indicates a denser packing of pellets near the wall.

The impact of the wall effect is particularly significant for small- to medium-sized induration pots commonly used in pelletizing plants. In such reactors, the wall-affected zone can occupy a substantial portion of the total volume. This non-uniform voidage distribution caused by the wall effect significantly influences fluid, heat, and mass transfer characteristics within the reactor bed. These factors and their implications on reactor performance will be explored in detail in the following.

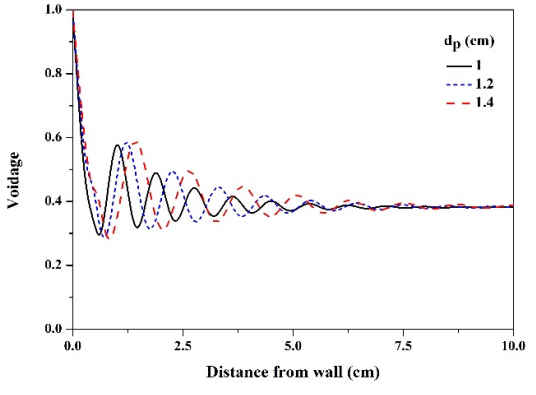

Fig. 5. Radial voidage variation according to Eq.(14) for the different particle diameters (d_p) in the packed bed of d_b equals 26.5 cm.

The heterogeneous voidage distribution induced by the wall effect (see Fig. 5.) significantly affects fluid, heat, and mass transfer within the reactor bed. Fig. 6. showcases contour plots of simulated bed temperature at various times (5, 9, 13, and 23 minutes) after the process begins. These plots reveal a noticeable radial temperature variation at different bed heights. The higher gas flow near the walls, a consequence of the wall effect, results in a faster temperature rise during the preheating and firing stages than in the center region. Conversely, during cooling, the wall zone cools down more quickly.

Comparing Fig. 5. (voidage distribution) with the temperature contour plots in Fig. 6. (at different times), we observe a trend: the thermal profiles become more uniform as we move further away from the reactor wall. This highlights a critical point - the pellets adjacent to the wall experience a distinct thermal history compared to those in the center of the bed. As a result, these wall-adjacent pellets cannot serve as a reliable benchmark for the reactor's overall temperature profile.

Building upon the observations regarding temperature profiles, Fig. 7. presents contour plots depicting the conversion fraction of magnetite to hematite at various times (5, 9, 13, and 23 minutes) after the process commences. Consistent with the temperature variations, the conversion fraction throughout the bed exhibits a spatial dependence. Across all process stages (preheating, firing, after-firing, and cooling), the conversion fraction increases with time, as expected. However, a crucial difference is observed: the conversion fraction near the wall consistently remains higher compared to the central zone. This disparity directly reflects the combined effects of temperature variations and varying gas flow rates across the reactor radius, as discussed earlier. As highlighted previously, the temperature and conversion ratio of pellets close to the wall (lateral) differ significantly from those in the center (central) throughout the reactor radius. Comparing the temperature profiles (Fig. 6.) with the conversion fraction profiles (Fig. 7.) provides a powerful tool for visualizing the spatial dependence of reaction progress within the reactor bed.

Fig. 8. delves deeper into the impact of the wall effect by quantifying the temperature difference between pellets near the wall (T_i) and those at the center (T'_i) at different heights (P_1, P_2, P_3) over time (as shown in Fig. 1). The observed trend can be broadly categorized into three stages:

Initial Rise (0-t_1): Initially, the temperature difference between lateral and central pellets increases rapidly. This is attributed to the higher gas flow near the walls, which leads to a faster rate of heat transfer to these pellets than in the central zone.

Peak and Decline (t_1-t_2): The temperature difference reaches a peak value (t_1) and then starts to decline. This indicates a diminishing wall effect as the bed's overall temperature increases. As the central region heats up, the disparity in heat transfer rates between the zones lessens.

Cooling Stage (t_2 onwards): During cooling, the temperature difference reverses. The upper region (P_1) shows a larger difference than the bottom (P_3) due to the upward flow of the cooling gas. This upward flow leads to faster cooling near the top, resulting in a more pronounced temperature difference between the wall and central zones.

As discussed previously, the temperature and gas flow near the reactor wall differ significantly from those in the center. This non-uniform environment has a direct consequence on the reaction kinetics, particularly the rate of magnetite oxidation to hematite.

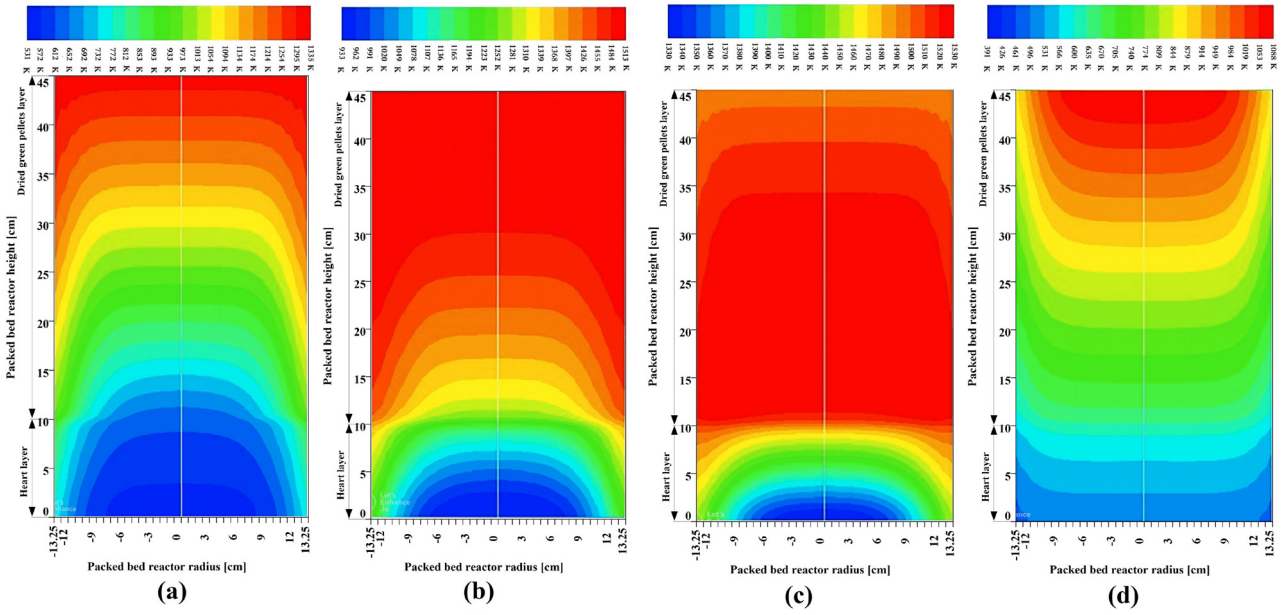

Fig. 6. Contour plots of bed temperature, based on simulation outputs, after:
(a) 5, (b) 9, (c) 13, and (d) 23 minutes from the beginning of the process.

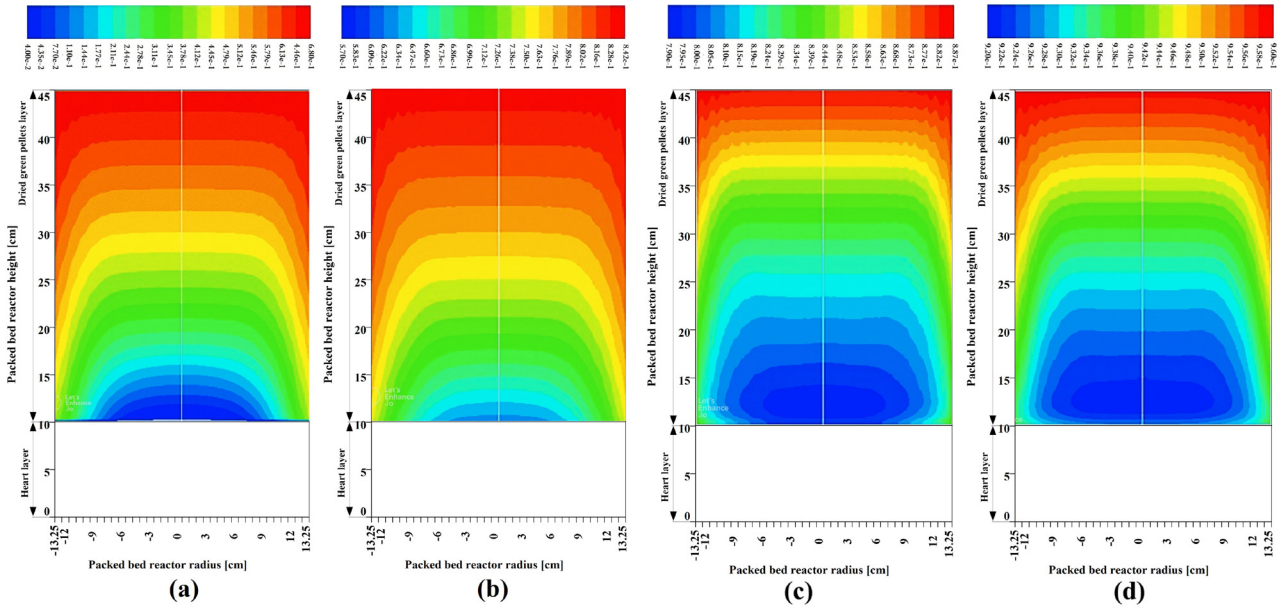

Fig. 7. Counter plots of the conversion fraction in the oxidation reaction of magnetite to hematite at (a) 5, (b) 9, (c) 13, and (d) 23 minutes from the beginning of the process.

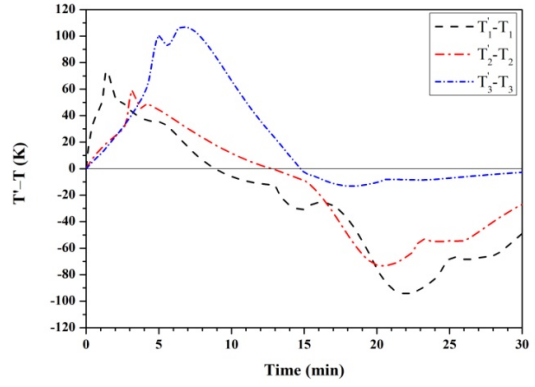

Fig. 8. Temperature difference between the side and central pellets at different heights.

Fig. 9. depicts the difference in conversion fraction (X_i-X'_i) between lateral pellets (X_i) close to the wall and central pellets (X'_i) at different heights (P_1, P_2, P_3) over time (refer to Fig. 1. for point designations). The significant difference observed throughout the process underscores the impact of varying temperature and gas flow profiles across the reactor radius. Higher temperatures and gas flow near the walls promote a faster magnetite conversion rate than in the central zone. This explains the consistently higher conversion fraction observed near the walls throughout the process.

It is important to note that the trend in the conversion fraction difference might not perfectly mirror the temperature difference (Fig. 8.). The conversion process also depends on the availability of oxygen in the passing gas. As the reaction progresses, the oxygen concentration near the walls might deplete at a faster rate due to the higher reaction rate. This could lead to a slight narrowing of the conversion fraction difference between the lateral and central regions in the later stages.

The aforementioned discussion of the spatially varying temperature and conversion history of pellets within the reactor bed (in the radial direction) is crucial. These variations can lead to differences in their final mechanical and metallurgical properties.

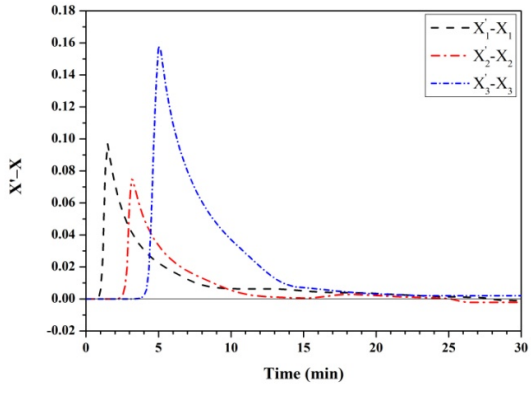

Fig. 9. Difference in the conversion fraction of the oxidation reaction of magnetite to hematite at the lateral and central points.

3.3. Comparison of Experimental Results of Pellet Properties at Walls and Centers of a Pellet Firing Pilot-Plant

The observations from the previous sections highlight the significant variation in thermal profiles within the reactor bed due to the wall effect. This non-uniform temperature distribution is likely to influence

the final properties of the hardened pellets.

To validate this hypothesis, an induration experiment was conducted, replicating the conditions employed in the Gol-E-Gohar firing unit number one. After sintering, pellet samples were collected from designated points within the bed (Fig. 1.). These points included P_1, P_2, and P_3 along the vertical axis and P'_1, P'_2, and P'_3 located one pellet distance from the furnace wall.

The collected pellets were subjected to experiments to determine their chemical composition and mechanical strength. Chemical analysis was performed using atomic absorption (total iron) and titration (residual FeO) methods. For mechanical strength evaluation, 35 pellets in good physical condition (free of cracks and other apparent defects) were selected and tested using a cold mechanical strength-testing apparatus. The average mechanical strength of these samples is reported as the mean cold mechanical strength. Additionally, the standard deviation is provided as a statistical measure to understand the dispersion of the test results. Table 1. summarizes the experimental findings. This approach allows for a direct comparison of pellet properties across different locations within the reactor bed, providing valuable insights into the impact of the wall effect on the final product.

Table 1. clearly demonstrates a substantial disparity in the reaction fraction (conversion) and mechanical strength of pellets collected from points near the wall (P'_1, P'_2, P'_3) compared to their counterparts in the central zone (P_1, P_2, P_3). This observation underscores the critical role of the wall effect on pellet properties within the reactor bed.

If sampling procedures in pilot plants are not meticulously designed to account for the wall effect, the results of various analyses can be misleading. These analyses include chemical composition (total iron, residual FeO), mechanical strength, abrasion resistance, crushing behavior, and reducibility. To mitigate the wall effect's influence on sampling and analysis, a more robust approach is recommended. This method involves using a metal cylinder that enters the top of the reactor bed after sintering. A vacuum sampler integrated into the cylinder can then extract samples uniformly from the central compartment, effectively avoiding pellets that the wall effect may impact.

This improved sampling strategy can significantly reduce the influence of non-uniform properties on analysis results, leading to more accurate data that better represent the overall characteristics of the produced pellets.

4. Conclusions

This study offers in-depth insights into the thermal and chemical behavior of iron ore pellets during induration, emphasizing the crucial impact of wall effects and radial variations in voidage on process performance. The key findings are as follows:

- A novel two-dimensional, axisymmetric CFD model was developed to simulate the induration behavior of iron ore pellets in a pilot-scale packed-bed furnace, incorporating radial variations in voidage, which were found to affect pellet temperature and reaction kinetics significantly.
- The model demonstrated that the wall effect led to a non-uniform voidage distribution, which, in turn, caused:
  A 20% temperature difference between pellets near the wall (P_1) and those in the center (P_3) at different radial positions.
  5%, 3%, and 6% Mean Relative Errors (MRE) for temperature measurements at P_1, P_2, and P_3, respectively, when compared to experimental data.
- Simulated and experimental results revealed that:
  The conversion fraction (magnetite to hematite) near the furnace wall was higher than in the central regions, with a significant disparity of up to 0.05 in conversion.
  The highest FeO content was measured at the center (P_3) compared to the lateral pellets (P'_3), confirming the spatial dependence of pellet conversion and oxidation rates on temperature and gas flow variations.
- The impact of radial voidage variation on temperature and reaction kinetics was highlighted, with:
  Higher gas flow rates near the walls lead to faster reaction rates in lateral pellets.
  A faster temperature rise in pellets closer to the wall during the preheating and firing stages.
- The proposed novel sampling method using a hollow metal cylinder with a vacuum sampler, inserted post-

Table 1. Comparison of Experimental Results of Pellet Properties at Walls and Centers of a Pellet Firing Pilot-Plant

	Total Fe (%)	Residual FeO (%)	Conversion Fraction	CCS (Kg/Pellet)	Standard Division (Kg/Pellet)
P_1	66.81	4.00	0.81	177	61.9
P'_1	66.96	3.84	0.82	199	50.2
P_2	66.93	3.12	0.85	151	60.7
P'_2	66.90	2.78	0.87	207	75.8
P_3	66.51	2.53	0.88	205	57.8
P'_3	66.95	2.93	0.86	216	47.6

sintering, effectively avoided wall-affected pellets and provided more accurate data for process optimization and quality control.

- The study provides a better understanding of the spatial variations in temperature and conversion within the reactor, which is critical for ensuring consistent pellet quality across different operational scales.
- The model's predictions are validated against pilot plant data, demonstrating its reliability and providing valuable insights for optimizing the pelletizing process while reducing the need for extensive pilot testing.

Acknowledgments

The authors gratefully acknowledge the Golgohar Iron Ore and Steel Company for providing the laboratory equipment. We also extend our thanks to Mr. Mehdi Azizkarimi for his constructive comments, and to Dr. Nima Sadeghi and Commander Dariush Darvishi for their generous help in revising this document.

Nomenclature

A) Latin Symbols

Symbol	Description	Unit
C_{O_2}	oxygen concentration in the gas	kg·m⁻³
$C_{O_2}^{eq}$	equilibrium oxygen concentration in the gas	kg·m⁻³
c_P	pellet heat capacity	J·kg⁻¹·K⁻¹,
$c_{p,g}$	gas specific heat capacity	J·kg⁻¹·K⁻¹
D_{O_2}	Oxygen diffusion coefficient	m²·s⁻¹
d_p	pellet diameter	m
h_c	overall heat transfer coefficient	W·m⁻²·K⁻¹
H_i	heat of reaction	J·mol⁻¹
h^*	both convective and radiative heat transfer coefficients	W·m⁻²·K⁻¹
k_{1st}	first-order rate constant for magnetite oxidation	s⁻¹
M	molar mass	kg·mol⁻¹
P	gas pressure	Pa
R	universal gas constant	J·mol⁻¹·K⁻¹
$\dot{R}$	source/sink term for species i	kg·m⁻³·s⁻¹
r_{mag}	radius of the magnetite pellet	m
r_g	pore radius	m
T_g	gas temperature	K
u	superficial gas velocity vector	m·s⁻¹
Y_i i	mass fraction of species	-

B) Greek Symbols

Symbol	Description	Unit
$\varepsilon_{(r)}$	local bed voidage	-
μ	gas viscosity	Pa·s
ρ_g	gas density	kg·m⁻³
ρ_P	pellet density	kg·m⁻³
ρ_{mag}	Magnetite density	kg·m⁻³

C) Dimensionless Numbers

Symbol	Description	Definition
Re_p	Reynolds number for pellet	$\rho_g u d_p / \mu$
Pr	Prandtl number for gas	$C_{p,g} \mu / k_g$
Sc	Schmidt number	$\mu / \rho_g D_m$
Nu	Nusselt number for pellet	$h_c d_p / k_g$
Sh	Sherwood number for pellet	$k_g d_p / D_m$

D) Abbreviations

Abbreviation	Description
CFD	Computational Fluid Dynamics
DEM	Discrete Element Method
USCM	Unreacted Shrinking Core Model
GAMG	Geometric Algebraic Multigrid
PISO	Pressure-Implicit with Splitting of Operators

References

[1] Halt J.A, Silva B.B, Kawatra S.K Miner, Process Extr Metall Rev. 2015; 36: 377.
[2] Forsmo S, Int J Miner Process. 2005; 75: 135.
[3] Forsmo S, Forsmo S,E, Samskog P,O, Björkman B, Powder Technol. 2008; 183: 247.
[4] Zhu D, Mendes V, Chun T, Pan J, Li Q, Li J, et al. ISIJ Int. 2011; 51(2): 214.
[5] Sarda A, Nithesh N, Krishna N, Shrivastva T, Prabhu A. 2014; 3(2): 10.
[6] Barati M, Int J Miner Process. 2008; 89: 30.
[7] Fan X.h, Yang G.m, Chen X.l, Gao L, Huang X.x, et al. Comput Chem Eng. 2015; 79: 80.
[8] Sadrnezhaad S, Ferdowsi A, Payab H, Comput Mater Sci. 2008; 44: 296.
[9] Küçükada K, Thibault J, Hodouin D, Paquet G, Caron S, Can Metall Q. 1994; 33: 1.
[10] Vortmeyer D, Winter R, Chem Eng Sci. 1984; 39: 1430.
[11] Bey O, Eigenberger G, Chem Eng Sci. 1997; 52: 1365.
[12] Geissbühler L, Zavattoni S, Barbato M, Zanganeh G, Haselbacher A, et al. CHIMIA. 2015; 69: 799.
[13] Zhang Z, Guo Z, Ji S, J Energy Chem. 2015; 24: 23.
[14] Nouri S, Ebrahim H.A, Jamshidi E, Chem Eng J. 2011; 166: 704.
[15] Pahlevaninezhad M, Emami M.D, Panjepour M, Energy. 2014; 73: 160.
[16] Sardari A, Alamdari E.K, Noaparast M, Shafaei S.Z, Int J Miner Metall Mater. 2017; 24: 486.
[17] Yur'ev B.P, Dudko V.A, Nikonenko E.A, Russ Metall (Met). 2022; 5: 481.
[18] Salmani M, Alamdari E.K, Firoozi S, J Therm Anal Calorim. 2017; 128: 1385.
[19] Chen Z, Zeilstra C, Van Der Stel J, Sietsma J, Yang Y, Ironmak Steelmak. 2020; 47: 741.
[20] Xing L, Qu Y, Wang C, Shao L, Zou Z, et al. Metall Mater Trans B. 2020; 51: 395.
[21] Alonso A, Lázaro M, Lázaro P, Lázaro D, J, Therm Anal Calorim. 2019; 138: 2703.
[22] Chen Z, Zeilstra C, Van Der Stel J, Sietsma J, Yang Y, ISIJ Int. 2020; 60: 65.
[23] Amani H, Alamdari E.K, Ale Ebrahim H, Estupinan A, Peters B, J Therm Anal Calorim. 2022; 147: 2293.
[24] Sardari A, Keshavarz Alamdari E, Noaparast M, Shafaei Z, Int J Min Geo-Eng. 2020; 54: 27.
[25] Zhang H, Bai K, Liu W, Chen Y, Yuan Y, Zuo H, et al. ISIJ Int. 2022; 62: 1792.
[26] Zheng H, Daghagheleh O, Ma Y, Taferner B, Schenk J, Kapelyushin Y, Metall Mater Trans B. 2023; 54: 1195.
[27] Gupta N, Sekhar C, Basha S.M, Kadhe D.M, Nallamilli M, Dwarapudi S, et al. Min Metall Explor. 2022; 39: 805-21.
[28] Amani H, Alamdari E.K, Moraveji M.K, Peters B, Particuology. 2024; 93: 75.
[29] Amani H, Alamdari E.K, Moraveji M.K, Estupinan A, Peters B, Ironmak Steelmak. 2022; 49: 615.
[30] Dave S, Patra S, Bapat Y, Banerjee G, Chattopadhyay S, JOM. 2023; 75: 2406.
[31] Duan S, Ding N, Wang S, Li B, Therm Sci. 2024; 00: 87.
[32] Küçükada K, Thibault J, Hodouin D, Paquet G, Caron S, Can Metall Q. 1994; 33: 1.
[33] Eppinger T, Seidler K, Kraume M, Chem Eng J. 2011; 166: 324.
[34] Zare Ghadi A, Valipour M.S, Biglari M, Ironmak Steelmak. 2016; 43: 418.
[35] Schotte W, AIChE J, 1960; 6: 63.
[36] Papanastassiou D, Bitsianes G, Metall Trans. 1973; 4: 477.
[37] Thurlby J, Metall Trans B. 1988; 19: 103.
[38] Fuller E.N, Schettler P.D, Giddings J.C, Ind Eng Chem. 1966; 58: 18.
[39] de Klerk A, AIChE J. 2003; 49: 2022.